http://dx.doi.org/10.1097/mm9.0000000000000036

MedMat

Original Research

OPEN

Biobased Ag nanowire films with high antibacterial activity for infected wound healing

Xueqian Li[a,b], Mi Chen[a], Bingshuai Jing[c], Jie Tian[d], Huidong Xie[b], Hailong Xu[a], Wenfeng Li[d], Mengqi Shen[e], Xiaona Ning[f,*], Wenhao Zhou[a,*], Hu Liu[d,*]

Abstract

Wound infection remains a critical challenge in clinical practice, frequently leading to delayed healing and increased risks of complications. Herein, we first screened silver nanowires (Ag NWs) with excellent antibacterial, antioxidant, and cell migration-promoting properties from silver-based nanomaterials with distinct dimensional morphologies, including Ag nanowires (NWs), Ag nanoparticles (NPs), nitrogen-doped graphene (NGC) supported Ag nanoparticles (Ag NPs/NGC), and Ag single atoms (Ag_1/NGC), as candidates for wound dressing applications. To further enhance therapeutic efficacy, we developed a composite film (Ag NWs@SF) by incorporating Ag NWs into silk fibroin (SF). Under near-infrared light, it generates localized heat to provide a synergistic antibacterial effect to accelerate wound healing. Interestingly, the robust electrical stimulation responsiveness of Ag NWs endows the film with the potential for real-time wound monitoring. This composite film demonstrates outstanding antibacterial activity against common wound pathogens, which maintains biocompatibility and fostering tissue regeneration. In vitro and in vivo studies reveal that the Ag NWs@SF membrane accelerates wound closure by stimulating cell migration, mitigating bacterial infection, and reducing inflammatory responses. These findings offer a novel approach for effective clinical wound management, potentially addressing the unmet clinical needs in infection combating and wound healing promoting.

Keywords: Ag-based nanomaterials, Film, Photothermal antibacterial, Wound healing, Wound infections

1. Introduction

Wound healing is a complex biological process involving tissue repair and regeneration, which is crucial for restoring the skin's barrier function[1]. However, severe wound infections remain a significant challenge in clinical practice[2]. Chronically infected wounds are typically associated with prolonged healing duration[3], increased risk of complications, and in severe cases, may lead to amputation or even death[4,5]. Consequently, there is an urgent need for effective strategies to manage infections and promote tissue regeneration simultaneously in patients with severe wound infections. Apart from antibiotics, current clinical approaches mainly rely on traditional dressings[6]. Due to relatively simple structures, these dressings are difficult to fully meet the multiple needs of complicated wounds and require frequent replacement[7]. Such limitations not only hinder real-time monitoring of wound status but also pose a risk of secondary tissue damage during dressing changes[8]. Thus, the development of novel functional dressings with integrated capabilities including broad-spectrum antibacterial activity, cell proliferation promotion, and real-time wound healing status monitoring, is urgently demanded.

Silver nanomaterials have been proved to exhibit broad-spectrum antimicrobial properties[9]. These nanomaterials can gradually release silver ions, which disrupt microbial cellular activities by interfering with protein synthesis, damaging cell membranes, inhibiting energy metabolism, and ultimately causing DNA damage[10–12]. Among numerous silver nanomaterials, including silver nanoparticles (Ag NPs), silver nanowires (Ag NWs), nitrogen-doped graphene-supported silver nanoparticles (Ag NPs/NGC), and silver single atoms (Ag_1/NGC), we have demonstrated Ag NWs possess excellent antibacterial activity and antioxidant properties, making them particularly promising for wound management. (Scheme 1A). As an important class of silver nanomaterials, Ag NWs have been approved by the U.S. Food and Drug Administration (FDA)[13,14]. Their high aspect ratio and slower release of silver ions result in lower toxicity to mammalian cells while maintaining high toxicity to microorganisms, making them suitable for integrating into biomedical devices. Ag NWs also exhibit exceptional photothermal properties, high conductivity, flexibility, and stability[15,16]. Photothermal therapy (PTT), which converts light energy into heat under

[a]*Shaanxi Key Laboratory of Biomedical Metallic Materials, Northwest Institute for Nonferrous Metal Research, Xi'an, China,* [b]*School of Chemistry and Chemical Engineering, Xi'an University of Architecture and Technology, Xi'an, China,* [c]*State Key Laboratory of Oral & Maxillofacial Reconstruction and Regeneration, National Clinical Research Center for Oral Diseases, Shaanxi Clinical Research Center for Oral Diseases, Department of Oral and Maxillofacial Surgery, School of Stomatology, The Fourth Military Medical University, Xi'an, China,* [d]*Key Laboratory of Green and High-end Utilization of Salt Lake Resources, Qinghai Engineering and Technology Research Center of Comprehensive Utilization of Salt Lake Resources, Qinghai Institute of Salt Lakes, Chinese Academy of Sciences, Xining, China,* [e]*Lenfest Center for Sustainable Energy, Columbia University, New York, USA,* [f]*Department of Ophthalmology, Tangdu Hospital, Fourth Military Medical University, Xi'an, China.*

**Corresponding authors: Address: Xiaona Ning, Department of Ophthalmology, Tangdu Hospital, Fourth Military Medical University, Xi'an 710038, China. E-mail address: ningxiaona0223@163.com (X. Ning); Wenhao Zhou, Shaanxi Key Laboratory of Biomedical Metallic Materials, Northwest Institute for Nonferrous Metal Research, Xi'an 710016, China. E-mail address: zhouwh@c-nin.com (W. Zhou); Hu Liu, Key Laboratory of Green and High-end Utilization of Salt Lake Resources, Qinghai Engineering and Technology Research Center of Comprehensive Utilization of Salt Lake Resources, Qinghai Institute of Salt Lakes, Chinese Academy of Sciences, Xining, Qinghai 810008, China. E-mail address: liuhu@isl.ac.cn (H. Liu).*

Xueqian Li and Mi Chen contributed equally to this work.

Supplemental Digital Content is available for this article.

MedMat (2026) 3:1

Received: 27 September 2025; Accepted 2 December 2025

Published online 5 January 2026

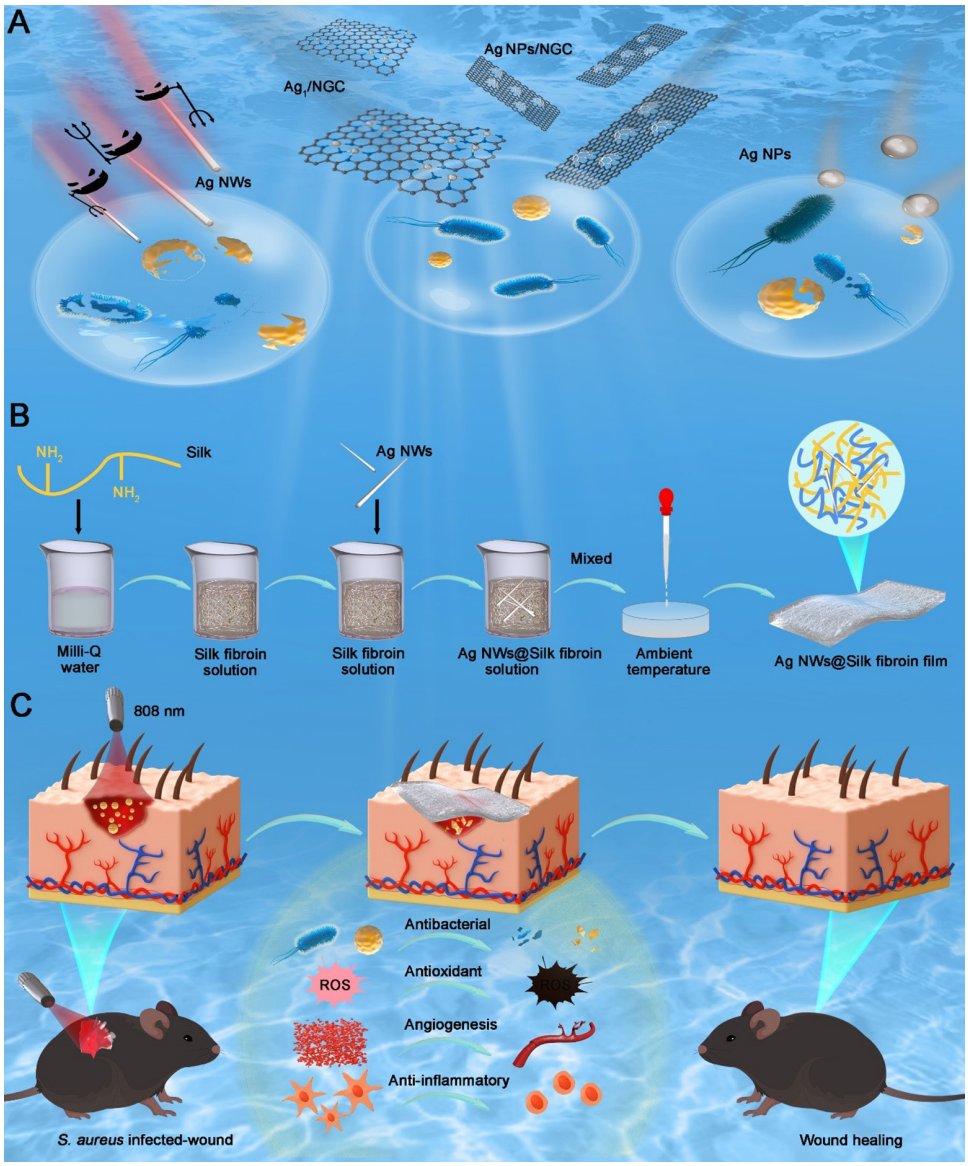

Scheme 1. Silver nanowire biobased composite films for wound healing and skin regeneration. (A) Antibacterial effects of silver nanomaterials with varying sizes and morphologies (Ag NWs, Ag1/NGC, Ag NPs/NGC, Ag NPs). (B) Production process of silk fibroin films embedded with silver nanowires. (C) Overview of the multifunctionality and potential applications of silver nanowire-embedded silk fibroin films in wound healing.

specific wavelengths, offers advantages such as controllable intensity, no risk of resistance, deep tissue penetration, and excellent biocompatibility, making it an ideal strategy to kill bacteria without using antibiotics[17]. However, a notable challenge is that PTT-assisted antibacterial agents typically require relatively high temperatures (>50 °C), which may damage healthy tissue surrounding the infected area[18]. A feasible solution is to integrate PTT with other antibacterial agents to achieve a synergistic effect under mild hyperthermia temperatures (<48 °C), which can effectively eradicate bacteria and promote wound healing without harming surrounding tissues[19,20], including near-infrared (NIR)-responsive Ag NWs containing wound dressings. However, the direct application of Ag NWs without a carrier limits their ability to precisely target the wound site.

SF, a natural biopolymer derived from silkworms, has been shown to be a promising biomaterial for wound healing[21]. Silk-based medical devices, such as surgical sutures, have been extensively studied for human use[22]. Injectable silk protein (Silk Voice) has received FDA approval (2019) for treating vocal fold insufficiency, and silk fibroin scaffolds (SERI) have been approved for use as surgical meshes. SF's exceptional biocompatibility, biodegradability, and cell adhesion and growth-promoting ability make it an ideal ingredient for incorporating into wound dressings[23,24]. As a natural protein derived from silk, SF induces an acute and mild but limited inflammatory response and exhibits low fibrotic behavior, highlighting its potential in modulating wound healing and tissue repair[25]. Additionally, SF has been demonstrated to have hemostatic activity[26], a crucial procedure in wound healing, and triggering the coagulation cascade by binding to fibrinogen and platelets is the underlying mechanism[27]. However, the lack of sufficient antimicrobial properties makes SF-based dressings not suitable for the application in severe wound infections. Therefore, we innovatively utilized SF as the carrier for Ag NWs, and explored this combination's performance in incisional skin wounds in mice (Scheme 1B). In addition, the excellent electrical signal responsiveness of Ag NW gives it the potential to dynamically track changes in the wound microenvironment.

In this study, we explored the antimicrobial properties of Ag NWs with various sizes and morphologies, and ultimately selected Ag NWs as the ideal candidate for integration into SF-based wound dressings. By incorporating Ag NWs into SF, we

created a composite material (Ag NWs@SF) that not only provides sustained antibacterial effects but also exhibits excellent anti-inflammatory, antioxidant, and proangiogenic properties, effectively achieving rapid healing of infected wounds (Scheme 1C). Our findings offer critical insights into the potential applications of Ag NWs@SF composites in advancing sophisticated wound-care strategies, particularly for treating severely infected chronic wounds.

2. Results and discussion

2.1 Synthesis and morphological characterization of silver nanowires and silver nanoparticles

The synthesis of Ag NWs and Ag NPs involves a 1-pot method and a polyol reduction process (Figure 1A). For the synthesis of Ag NWs, the reaction system proceeded via a reflux polymerization approach, wherein the addition of $CuCl_2$ catalyzed the reduction of silver ions. Subsequent centrifugation and methanol washing removed unreacted species, yielding well-defined Ag NWs. Scanning electron microscopy (SEM) and transmission electron microscopy (TEM) images confirmed the nanowire (NW) morphology of the synthesized silver nanomaterials. High-resolution TEM (HR-TEM) analysis revealed lattice fringes with an interplanar spacing of d = 0.2353 nm, corresponding to the {111} plane of silver. The well-aligned lattice fringes and absence of grain boundaries or dislocations further confirmed the high-quality single-crystalline structure of the NWs (Figure 1B and Supplementary Figure 1, https://links.lww.com/MEDMAT/A6)[28]. Based on SEM analysis, the synthesized Ag NWs exhibited an average diameter distribution of 60–80 nm (Supplementary Figure 1, https://links.lww.com/MEDMAT/A6).

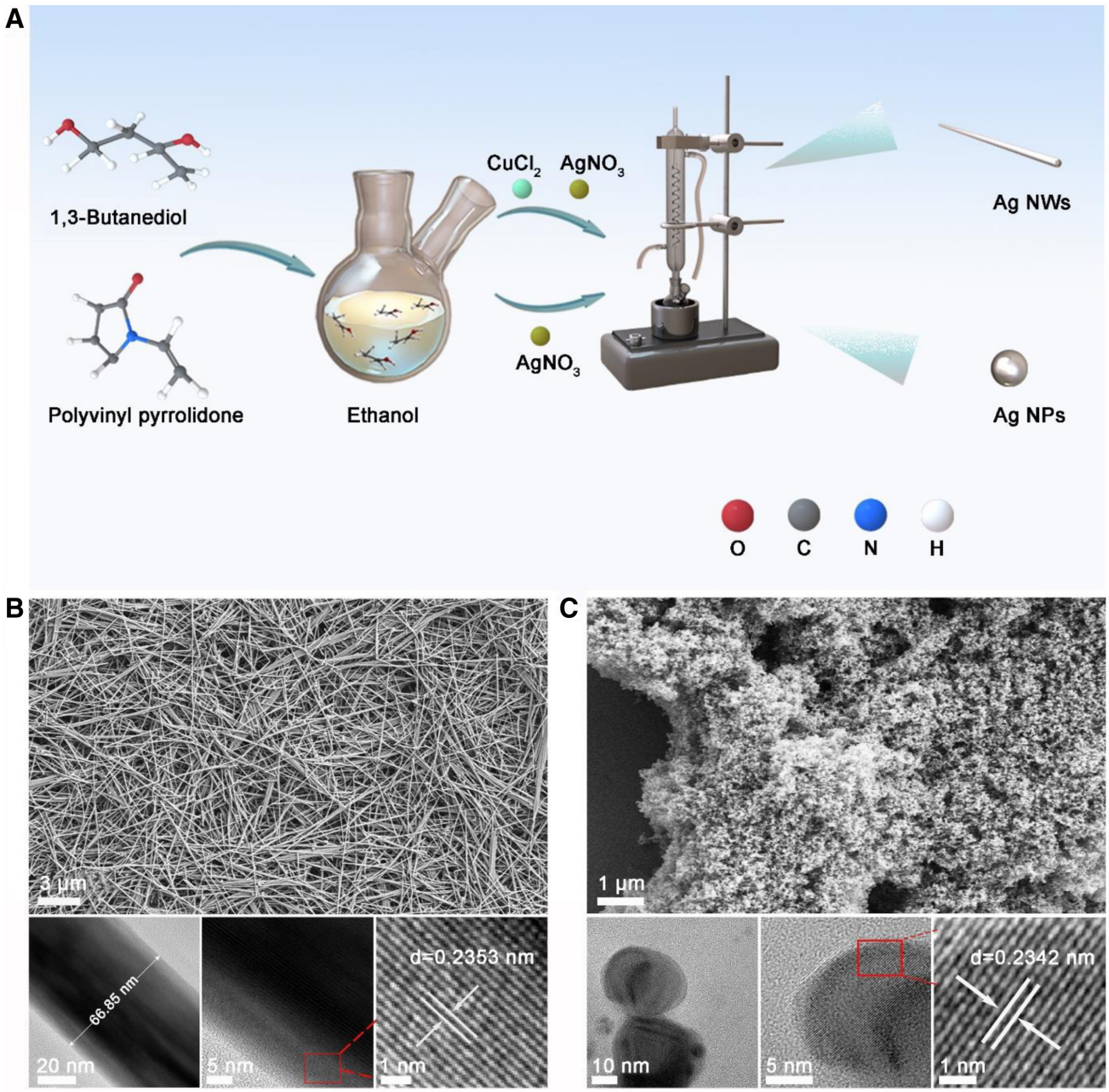

Figure 1. Synthesis and morphological characterization of materials. (A) Synthesis flowchart for Ag NWs and Ag NPs. (B) SEM, TEM, and HR-TEM images of Ag NWs. (C) SEM, TEM, and HR-TEM images of Ag NPs.

In contrast, the synthesis of Ag NPs follows a similar process, but without the addition of $CuCl_2$, reduction is solely achieved using $AgNO_3$. Through centrifugation and washing, Ag NPs are successfully obtained, exhibiting a highly uniform distribution in terms of morphology. Representative SEM, TEM, and HR-TEM images of the Ag NPs, taken at different magnifications, are shown in Figure 1C. The images reveal the edge regions of the particles, and upon further magnification, the surface structure of the crystals appears well-defined and smooth, indicating high crystallinity. Fourier transform (FFT) analysis of the lattice fringes and interplanar spacing of the Ag NPs yields a calculated spacing of 0.2342 nm, corresponding to the {111} plane of silver in its face-centered cubic (FCC) crystal structure. This plane is typically the most stable crystallographic facet for metallic Ag NPs. Corresponding energy-dispersive spectroscopy (EDS) mapping from scanning transmission electron microscopy (STEM-EDS) confirms the uniform distribution of silver within the nanoparticles (NPs; Figure 1C and Supplementary Figure 2, https://links.lww.com/MEDMAT/A6).

This study demonstrates the successful synthesis of both Ag NWs and Ag NPs. It provides an efficient and controlled synthetic route, which not only offers experimental data for the further application of silver nanomaterials but also serves as a valuable reference for the synthesis of other nanomaterials.

2.2 Synthesis and characterizations of Ag NPs/NGC and Ag_1/NGC

Silver nanomaterials with excellent dispersion and stability were synthesized by combining hydrothermal and pyrolysis strategies. These methods not only effectively control the morphology of silver but also improve the performance of silver-based catalysts through the support of nitrogen-doped carbon (NGC) materials. Initially, melamine powder was sonicated with an ethylene glycol aqueous solution in ethanol, followed by refluxing at 80 °C. This step aimed to form the basic structure of NGC, providing a suitable substrate for subsequent silver loading. Afterward, an $AgNO_3$ solution was added, and the reaction continued under reflux conditions. During this process, silver ions were reduced to form either Ag NPs or silver single atoms. The final product consists of Ag NPs/NGC and Ag_1/NGC (Figure 2A).

Representative TEM, HR-TEM, high-angle annular dark-field scanning transmission electron microscopy (HAADF-STEM), EDS, and elemental mapping images of the Ag NPs/NGC are presented (Figure 2B). TEM images display the distribution of Ag NPs/NGC, with the overall morphology resembling a sheet-like two-dimensional material (graphene sheets). The Ag NPs are evenly distributed on the nitrogen-doped graphene, with small particle sizes, and the dark spots can be identified as Ag NPs. The two-dimensional plane of nitrogen-doped graphene likely provides a stable substrate for the growth of Ag NPs. HR-TEM images and lattice analysis reveal the crystal structure of individual Ag NPs. The FFT analysis of the inserted image shows clear lattice fringes, indicating high crystallinity of the Ag NPs[29]. The interplanar spacing of d = 0.2154 nm corresponds to the {111} plane of silver, consistent with the FCC structure of silver. HAADF-STEM images further confirm the distribution of the Ag NPs. The bright areas correspond to regions with a higher atomic number silver (Ag), while the darker regions correspond to the graphene substrate, providing further evidence that the Ag NPs are uniformly loaded on the nitrogen-doped graphene surface. Corresponding EDS STEM-EDS mapping results show a homogeneous distribution of C, N, and Ag elements across the nitrogen-doped graphene network (Figure 2B).

TEM images reveal the overall structure of nitrogen-doped graphene with a scale bar of 50 nm. The nitrogen-doped graphene exhibits a layered two-dimensional structure. Upon magnification of the region marked by the red rectangle, HR-TEM images (Figure 2C) show that silver single atoms are uniformly distributed on the nitrogen-doped graphene (the positions of the Ag single atoms are marked by red circles). The dense distribution of red circles indicates that these Ag single atoms are well-dispersed without aggregation. The corresponding HAADF-STEM image reveals that, due to the higher atomic number of Ag, its signal appears as bright spots, whereas the graphene signal is weaker. The overall structure retains the basic morphology of the two-dimensional sheet-like material of the nitrogen-doped graphene composite. Elemental distribution maps from EDS show the uniform distribution of carbon (C, green), nitrogen (N, blue), and silver (Ag, red) across the nitrogen-doped graphene network. These maps confirm that C, N, and Ag are evenly distributed in the NW network of nitrogen-doped graphene, and no aggregation of Ag single atoms is observed.

In conclusion, the Ag NPs/NGC material exhibits a more uniform distribution of NPs, while the Ag_1/NGC material presents a single-atom level of silver loading. This study provides a simple and effective synthesis method for controlling the morphology of silver and loading it onto NGC materials.

2.3 Chemical structural characterization of nanomaterials

To further investigate the chemical structures of Ag NWs, Ag NPs, Ag NPs/NGC, and Ag_1/NGC, several characterization techniques, including X-ray photoelectron spectroscopy (XPS), Raman spectroscopy, and X-ray diffraction (XRD), were employed. First, for the Ag NPs/NGC sample, the C 1s XPS spectrum (Figure 3A) displays a signal peak at 284.9 eV, corresponding to C–C bonds. Additionally, the high-resolution N 1s XPS spectrum reveals peaks at approximately 401.08, 400.18, and 398.38 eV (Figure 3B), which are attributed to graphitic nitrogen, pyrrolic nitrogen, and pyridinic nitrogen, respectively, confirming the successful nitrogen doping of the NGC[30]. The Ag 3d XPS spectrum for the Ag NPs/NGC sample (Figure 3C) shows 2 main peaks at around 368.16 eV (Ag $3d_{5/2}$) and 374.13 eV (Ag $3d_{3/2}$), with a binding energy separation of 6 eV. The energy loss feature also aligns with the Ag^0 state, further confirming that silver exists in its metallic zero-valent form[31].

For the Ag_1/NGC, the C 1s XPS spectrum (Figure 3D) not only shows the C–C signal peak at 285.1 eV but also a signal at 287.8 eV corresponding to C–N bonds, indicating successful modification of nitrogen-doped graphene. The N 1s XPS spectrum (Figure 3E) reveals characteristic peaks at approximately 399.78 eV (graphitic N), 398.68 eV (pyrrolic N), 397.38 eV (pyridinic N), and 396.78 eV (Ag-N bond), confirming the successful anchoring of silver atoms on the nitrogen-doped graphene via coordination with nitrogen. Further Ag 3d XPS analysis (Figure 3F) shows the 2 main peaks at 368.27 eV (Ag $3d_{5/2}$) and 374.24 eV (Ag $3d_{3/2}$), along with the energy loss feature, confirming the zero-valent state of silver. No significant Ag^+ signal is observed, suggesting that silver exists solely in the Ag^0 form.

XRD and Raman spectroscopy analyses were performed to further confirm the atomic structure of Ag NPs/NGC and Ag_1/NGC. In the XRD spectra (Figure 3G), both Ag NPs/NGC and Ag_1/NGC show a graphene (002) diffraction peak at around 26.5 ° (Supplementary Figure 3, https://links.lww.com/MEDMAT/A6), confirming the presence of the graphene substrate. Notably, the Ag NPs/NGC sample also exhibits characteristic diffraction peaks of silver crystals, including 38.1° (111), 44.3° (200), and 64.4° (220) (Supplementary Figure 4, https://links.lww.com/MEDMAT/A6), indicating that silver is present as NPs with good crystalline structure. In contrast, no such silver crystal diffraction peaks are observed in the XRD spectrum of Ag_1/NGC, further supporting the idea that silver is dispersed as single atoms within the nitrogen-doped graphene matrix. Raman spectra for both Ag_1/NGC and Ag NPs/NGC display the characteristic D peak (around 1352 cm^{-1}) and G peak (around 1557 cm^{-1}) (Figure 3I). Specifically, the D/G ratio for Ag_1/NGC (1.33) is higher than that of Ag NPs/NGC (1.19), indicating a

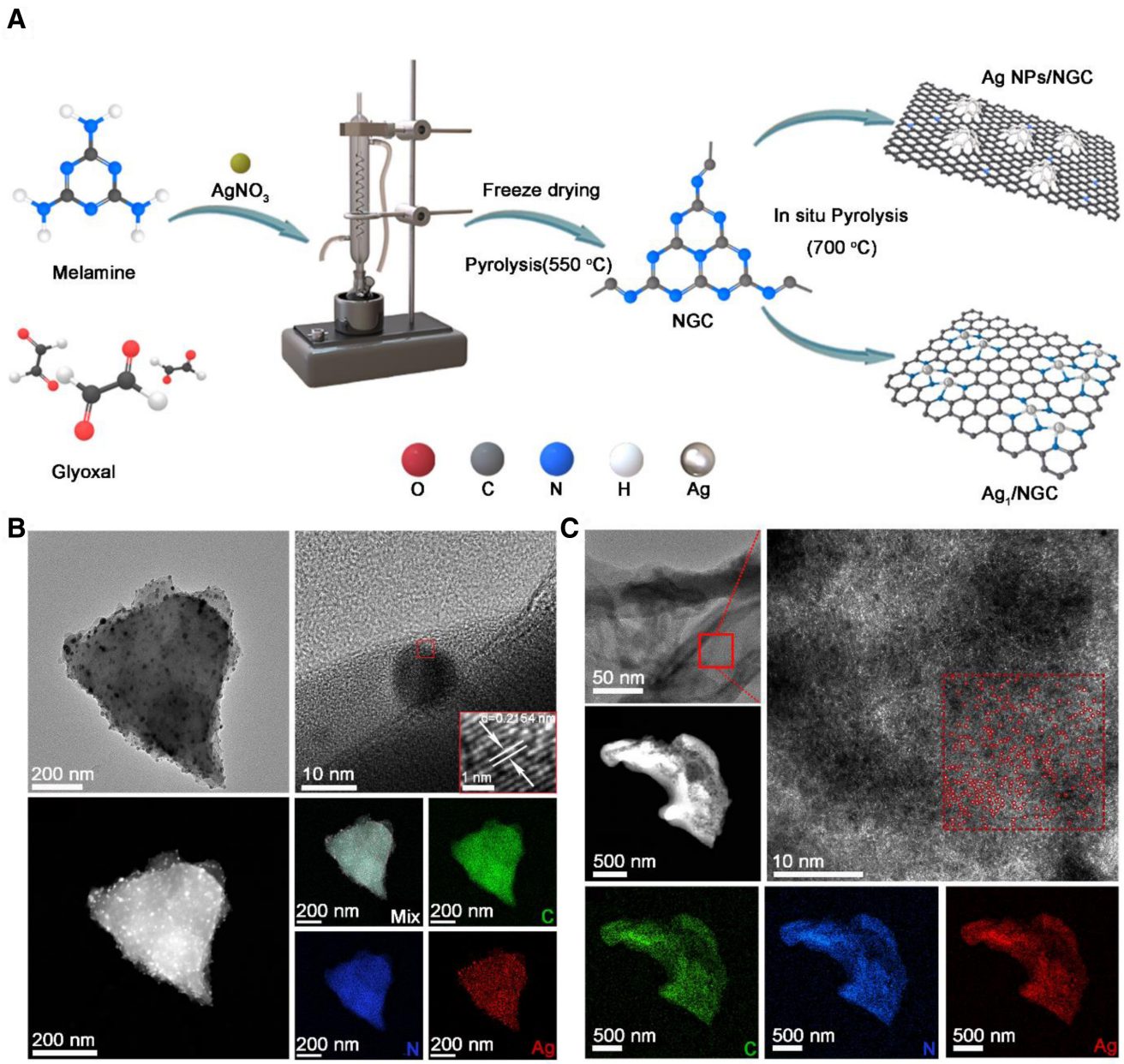

Figure 2. Structural and compositional characterizations of Ag NPs/NGC and Ag_1/NGC. (A) Design strategy for Ag NPs/NGC and Ag_1/NGC. (B) TEM images revealing the Ag NPs/NGC structure and EDS mappings of the elements (C, N, Ag). (C) TEM images revealing the Ag_1/NGC structure and EDS mapping of C, N, and Ag elements.

higher density of defects or disorder in Ag_1/NGC. This is consistent with the two-dimensional structural characteristics of nitrogen-doped graphene.

Finally, XRD analysis of Ag NWs and Ag NPs (Figure 3H) reveals that the main diffraction peaks for both Ag NWs and Ag NPs are located at around 38° (111), 44° (200), 64° (220), and 77° (311), which match the standard diffraction peaks for silver (Supplementary Figure 4, https://links.lww.com/MEDMAT/A6). The diffraction peaks exhibit clear symmetry without any spurious peaks, indicating that the synthesized Ag NWs and Ag NPs possess good crystallinity.

2.4 Antioxidant activities of Ag NWs, Ag NPs, Ag NPs/NGC, and Ag_1/NGC

The experimental results demonstrated that Ag NWs exhibited superior radical scavenging efficiency, showing the most significant DPPH scavenging rate among the tested materials. This observation was consistent with the pronounced color change of DPPH solution observed in (Supplementary Figure 5, https://links.lww.com/MEDMAT/A6), indicating that the radical scavenging capacity of Ag NWs significantly surpassed that of the other 3 silver-based nanomaterials. This enhanced performance may be attributed to the unique nanostructure and larger specific surface area of Ag NWs. The high aspect ratio of Ag NWs provides an extensive surface contact area, facilitating efficient interaction with free radicals and thereby enhancing antioxidant activity. Additionally, the zero-valent state of silver may play a crucial role in redox reactions, suggesting that the surface state of silver atoms in the NW structure could be a key factor contributing to its superior antioxidant performance. The remarkable DPPH radical scavenging capacity of Ag NWs indicates their potential in mitigating oxidative stress, promoting cellular repair, and improving the local microenvironment (Supplementary Figure 6,

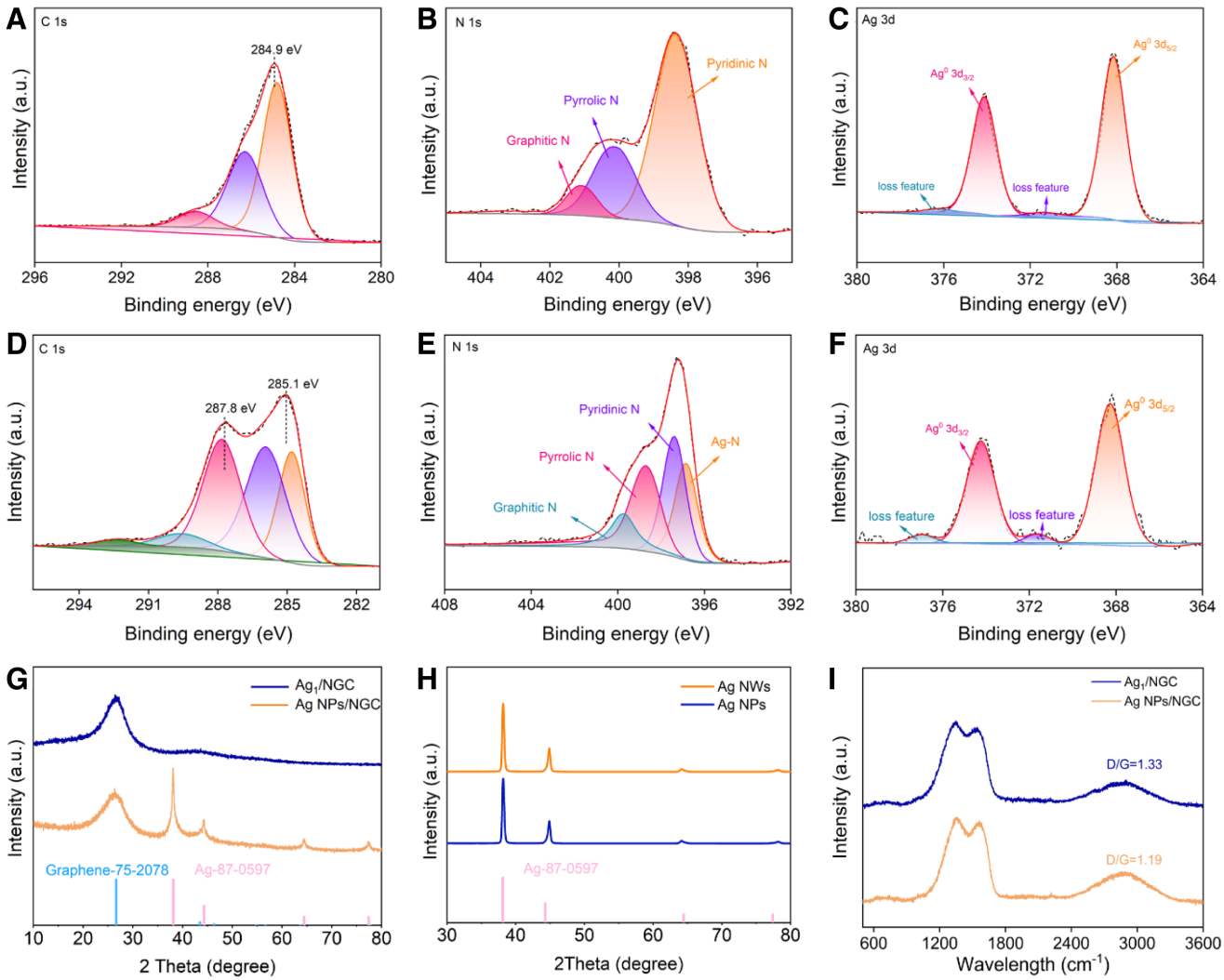

Figure 3. Chemical structural characterization of nanomaterials. (A) C 1s, (B) N 1s, and (C) Ag 3d XPS spectra in Ag NPs/NGC, respectively. (D) C 1s, (E) N 1s, and (F) Ag 3d XPS spectra in Ag_1/NGC, respectively. (G,H) XRD pattern, and (I) Raman spectra.

https://links.lww.com/MEDMAT/A6). By reducing free radical accumulation, these antioxidants not only protect cells from oxidative damage but also enhance cell proliferation and migration, promote collagen synthesis, reduce excessive inflammatory responses, and prevent scar formation[32,33]. Consequently, Ag NWs demonstrate significant potential in accelerating and improving the quality of wound healing, particularly in the treatment of chronic and severely infected wounds, suggesting promising clinical applications in wound management.

2.5 Antibacterial activities of Ag NWs, Ag NPs, Ag NPs/NGC, and Ag_1/NGC

Bacterial infections can significantly hinder wound healing[2]. The antibacterial properties of silver have inspired us to explore the antibacterial activity of Ag NPs with varying sizes and morphologies. To determine which of the synthesized 4 silver nanomaterials is most suitable for antibacterial dressings, we assessed the antibacterial properties of Ag NWs, Ag NPs, Ag NPs/NGC, and Ag_1/NGC using the agar plate method and zone of inhibition assay. Initially, we performed a zone of inhibition assay to screen the antibacterial activity of different amounts of Ag NWs, Ag NPs, Ag NPs/NGC, and Ag_1/NGC against *Staphylococcus aureus* at a concentration of 1 mg/mL (Supplementary Figure 7, https://links.lww.com/MEDMAT/A6 and Supplementary Figure 8, https://links.lww.com/MEDMAT/A6). The antibacterial effect of Ag NPs/NGC was found to be relatively weak. The antibacterial activity of Ag_1/NGC was also limited, possibly due to the well-dispersed nature of silver single atoms, resulting in fewer silver ions exposed on the surface and thus affecting its antibacterial efficacy. Ag NWs exhibited the best antibacterial performance.

Further antibacterial performance comparison was conducted using the agar plate method for different concentrations of Ag NWs and Ag NPs (Supplementary Figure 9, https://links.lww.com/MEDMAT/A6), which corroborated our initial conclusion. This result may be related to the high aspect ratio structure of Ag NWs, which can more effectively interact with bacterial cell surfaces due to their elongated morphology, thus enhancing their antibacterial activity. The large surface area of Ag NWs offers more silver ion release sites, disrupting the bacterial cell wall and membrane structure, leading to leakage of intracellular contents and inhibiting bacterial growth. At a concentration of 1 mg/mL, the antibacterial rate of Ag NWs was significantly superior to that of Ag NPs. Therefore, Ag NWs were selected as the focus for subsequent research.

2.6 Biocompatibility and cell migration evaluation of Ag NWs

In order to evaluate the biocompatibility and cell migration potential of Ag NWs, experiments on cell viability and death

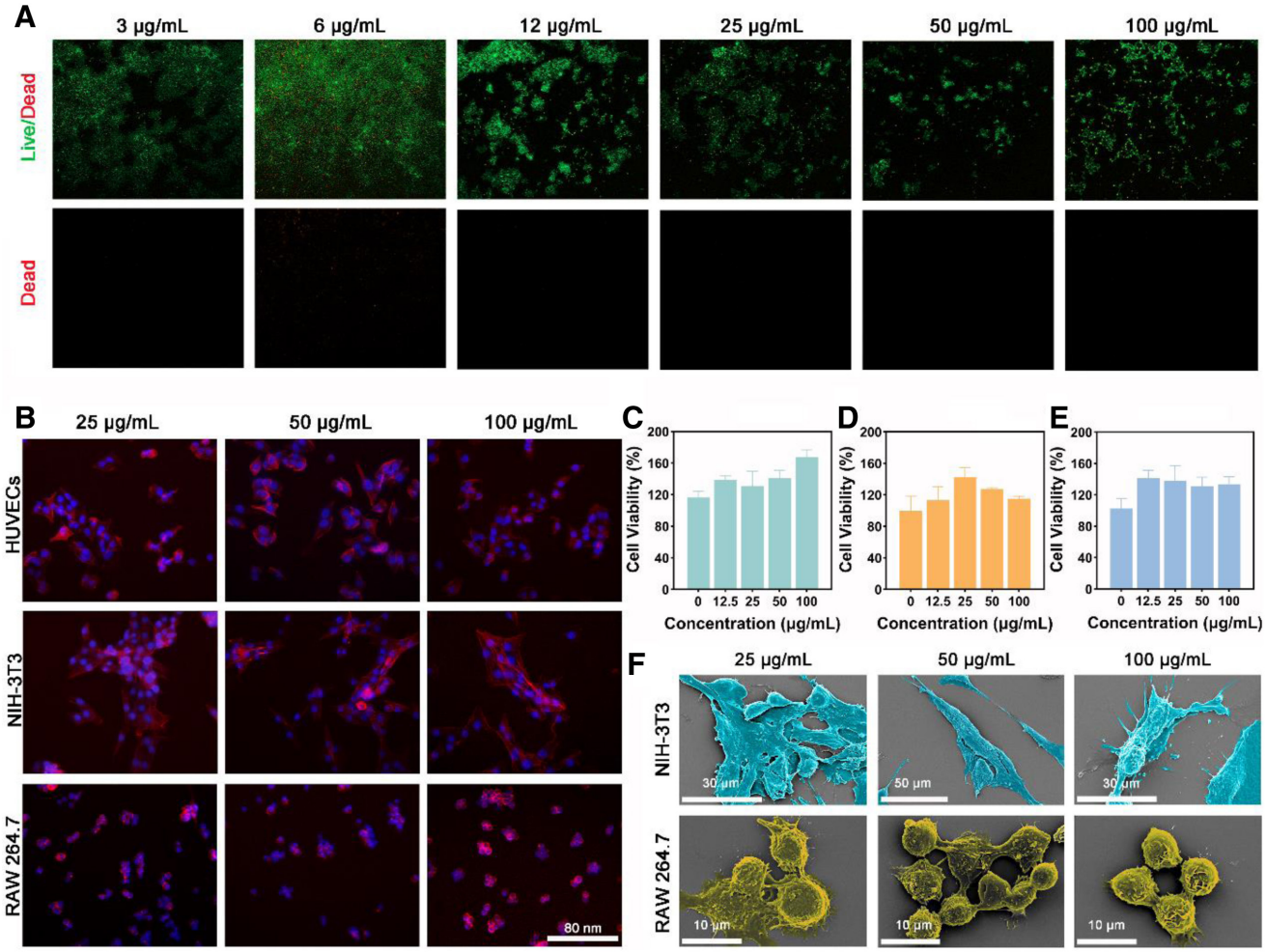

Figure 4. Cell compatibility of Ag NWs. (A) Live/dead staining of RAW 264.7 cells treated with Ag NWs. (B) Fluorescence staining of HUVECs, NIH-3T3, and RAW 264.7 cells treated with Ag NWs. (C) HUVECs cells, (D) NIH/3T3 cells, (E) RAW 267.4 cells, relative cell viability in response to Ag NWs (n = 6). (F) SEM images of RAW 264.7 and NIH-3T3 cells treated with Ag NWs.

staining as well as cell morphology observation, were conducted. Initially, cells were treated with different concentrations of Ag NWs, followed by viability and death cell staining analysis. As the concentration of Ag NWs increased, the cell viability was not significantly affected (Figure 4A). The majority of cells remained with green fluorescence (live cells), while only a small number of cells exhibited red fluorescence (dead cells), suggesting that Ag NWs demonstrated good biocompatibility within the tested concentration range.

Subsequently, human umbilical vein endothelial cells (HUVECs), mouse embryonic fibroblasts (NIH-3T3), and mouse macrophages (RAW 264.7) were treated with extraction solutions of Ag NWs at different concentrations. The cell morphology was observed by fluorescently labeling the cytoskeleton (red) and cell nucleus (blue) (Figure 4B). At concentrations of 25, 50, and 100 μg/mL, all 3 types of cells maintained normal morphology. No significant cytoskeletal breakage or nuclear fragmentation was observed, further demonstrating that Ag NWs had no obvious detrimental effects on cell morphology and structure. To further verify the impact of Ag NWs on cell viability, the viability of the 3 cell types treated with Ag NWs extraction solutions at different concentrations (up to 100 μg/mL) was determined (Figure 4C–E). The results showed that even at the highest concentration (100 μg/mL), the Ag NWs extraction solution did not significantly and adversely affect the viability of HUVECs, NIH-3T3, and RAW 264.7 cells. The cell viability of all treatment groups remained above 80%. Additionally, through a culture experiment lasting 1, 3, and 5 days (Supplementary Figure 10, https://links.lww.com/MEDMAT/A6–Supplementary Figure 12, https://links.lww.com/MEDMAT/A6), a proliferation trend was observed in all 3 cell types, further supporting the good biocompatibility of Ag NWs in in vitro experiments.

Cell migration is an essential process in wound healing, especially the migration of fibroblasts, which is crucial for tissue repair. To assess the influence of Ag NWs on cell migration, a scratch assay was employed to evaluate the promoting effect of Ag NWs on the migration of NIH-3T3 cells. After 24-h treatment, the cell migration in the Ag NWs group was significantly faster than that in the control group, and the degree of scratch area closure was significantly increased (Supplementary Figure 13, https://links.lww.com/MEDMAT/A6). Quantitative analysis results further confirmed this observation (Supplementary Figure 14, https://links.lww.com/MEDMAT/A6). At all concentrations (12.5, 25, 50, 100 μg/mL), Ag NWs significantly accelerated the migration of NIH-3T3 cells in the scratch area. Especially at a concentration of 100 μg/mL, the relative healing rate was significantly increased to 23.4% compared to the control group, which was only 6.6%. To more intuitively observe the changes in cell morphology, SEM was used to analyze the cell morphology (Figure 4F and Supplementary Figure 15, https://links.lww.com/MEDMAT/A6). The results indicated that the cells in the Ag NWs-treated group maintained good morphology, with significant pseudopod extension, clear surface microstructure,

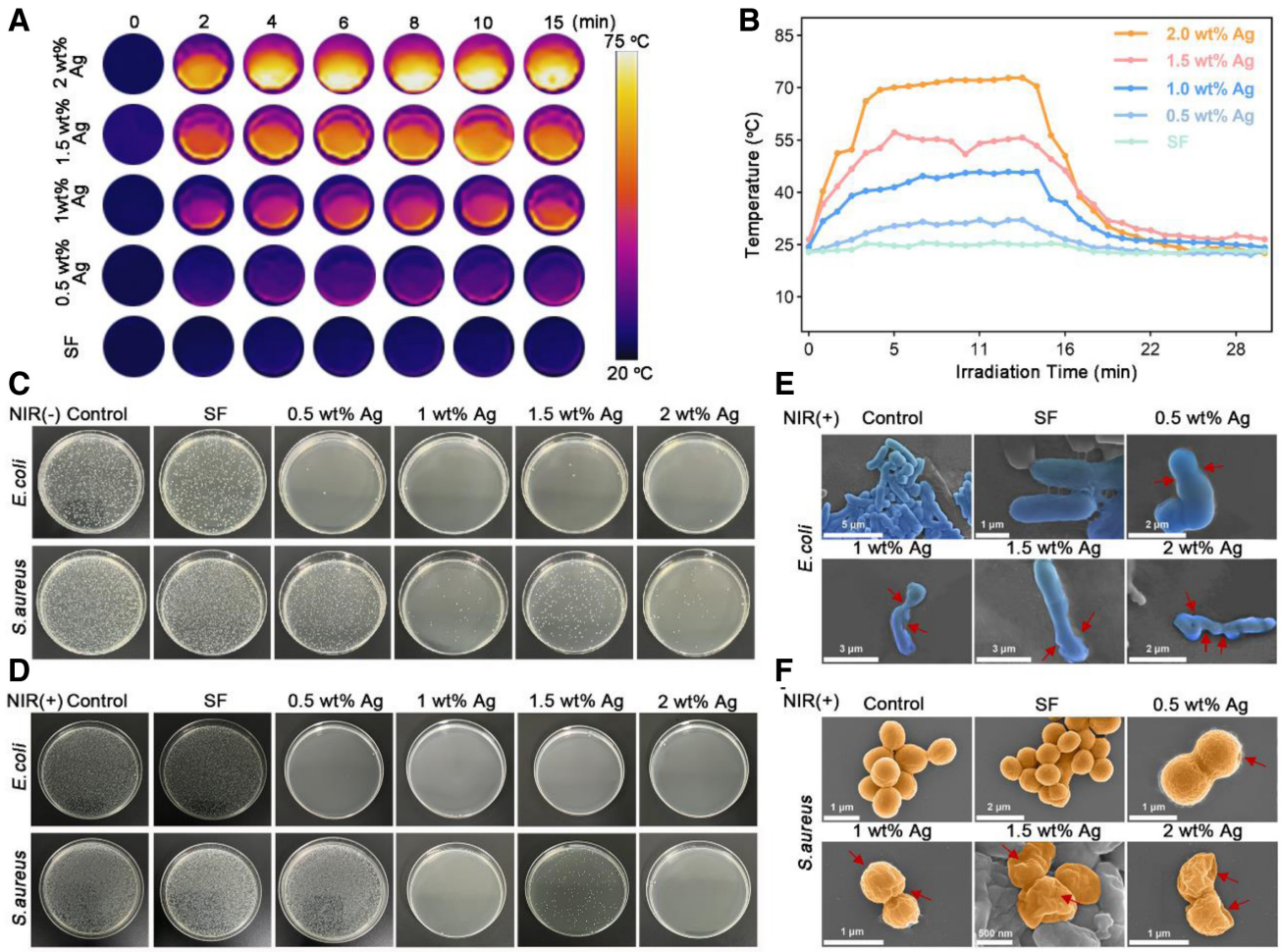

Figure 5. In vitro antibacterial activity of Ag NWs@SF film under near-infrared (NIR) irradiation. (A) Thermal infrared image of the Ag NW@SF membrane in PBS under NIR light irradiation (808 nm, 2.5 W/cm^2). (B) Temperature variation curve over time for the Ag NWs@SF membrane in PBS under NIR light exposure. (C) Representative plate samples of *Escherichia coli* and *S. aureus* cultured on Ag NWs@SF. (D) Representative plate samples of *E. coli* and *S. aureus* post-NIR irradiation (808 nm, 2.5 W/cm^2). (E) SEM images of *E. coli* following NIR treatment. (F) SEM images of *S. aureus* following NIR treatment.

and good cell spreading. However, as the concentration of Ag NWs increased, the degree of cell spreading slightly decreased, possibly due to the impact of certain surface properties of high-concentration Ag NWs on cell attachment.

In conclusion, Ag NWs exhibited excellent performance in both in vitro biocompatibility and cell migration. Ag NWs not only effectively promoted the NIH-3T3 but also contributed to the maintenance of cell viability and morphological stability, indicating their potential in wound healing. Moreover, the outstanding biocompatibility of Ag NWs renders it a wound-repair material with broad application prospects.

2.7 Antibacterial performance of Ag NWs@SF

Given the potential of silk fibroin (SF) in regulating wound healing and tissue repair, this study selected SF as a carrier for Ag NWs, aiming to achieve rapid sealing and repair of mouse skin incision wounds. Using SEM, mapping, and XPS characterization techniques, we confirmed that Ag NWs were encapsulated within the SF film (Supplementary Figure 16, https://links.lww.com/MEDMAT/A6–Supplementary Figure 18, https://links.lww.com/MEDMAT/A6). This encapsulation not only promotes the slow release of Ag NWs but also enhances the biocompatibility of the material, providing sustained antibacterial effects for wound repair.

In this study, PTT, as an antibiotic-free antibacterial approach, offers unique advantages. Mild PTT (<48 °C) can effectively eliminate bacteria while promoting wound healing, without causing damage to adjacent skin tissues. Thermal imaging analysis in phosphate-buffered saline (PBS) revealed that the pure SF film exhibited no significant temperature change under NIR light, indicating that SF itself does not possess substantial photothermal conversion capabilities. In stark contrast, the addition of Ag NWs significantly enhanced the photothermal effect. Specifically, materials with varying concentrations of Ag NWs exhibited different responses to NIR light (Figure 5A). As the Ag NW concentration increased, the photothermal response effect also showed an increasing trend. Temperature rise and fall tests conducted on different Ag NWs@SF films in PBS showed that the Ag NWs@SF films reached a stable temperature within a short time (<5 min), proving that Ag NWs are the primary photothermal conversion material. Moreover, under NIR irradiation, Ag NWs@SF films with doping concentrations of 0.5 wt% and 1.0 wt% satisfied the thermally induced antibacterial conditions (<48 °C) (Figure 5B).

To further verify this, we coincubated SF films with different Ag NW doping concentrations with *E. coli* and *S. aureus* for 3 h. The experimental results showed that the 1.0 wt% Ag NWs@SF film exhibited significantly improved antibacterial performance compared to both the blank group and the pure SF group (Figure 5C). Notably, NIR irradiation further enhanced the antibacterial effect (Figure 5D). This demonstrates that the synergistic effect between the photothermal effect and

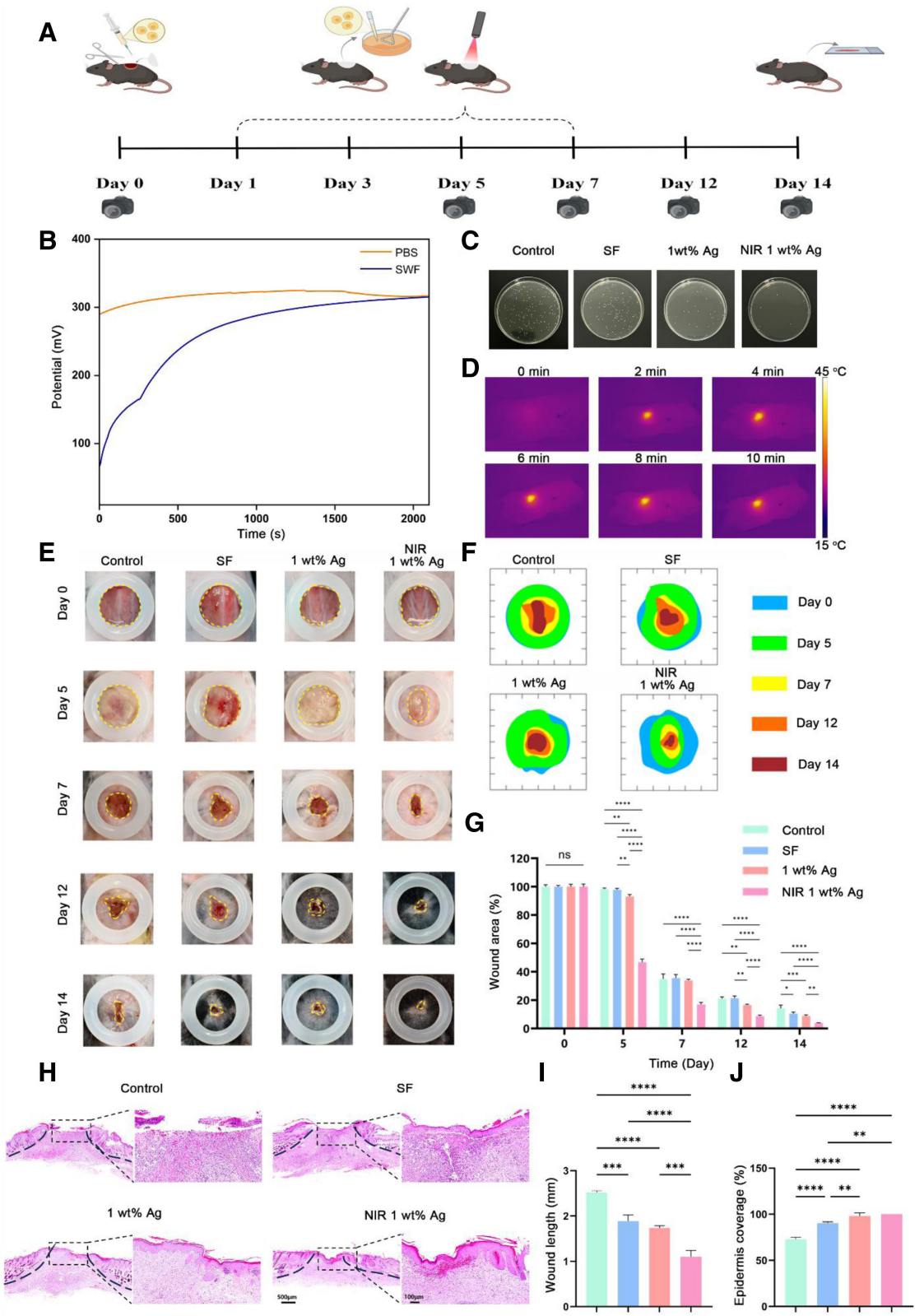

Figure 6. In vivo infected wound healing assay. (A) Experimental procedures performed at each time point. (B) Potential curves for Ag NWs@SF dressing in pure PBS and simulated exudate. (C) Antibacterial plating of wound tissue on day 3. (D) Thermal imaging of 808 nm near-infrared irradiation at 0.8 W/cm^2. (E) Wound healing is illustrated. (F) Wound traces at different periods of wound healing. (G) Wound healing rate of each group for different days. (H–J) Hematoxylin–Eosin (H&E) staining and quantitative analysis.

Ag NWs plays a crucial role in improving antibacterial activity. To further explore the mechanism of the antibacterial effect, we analyzed the morphological changes of the bacteria. SEM images after NIR irradiation revealed that the morphology of *E. coli* and *S. aureus* in the control group and pure SF group remained largely intact, with no significant destruction

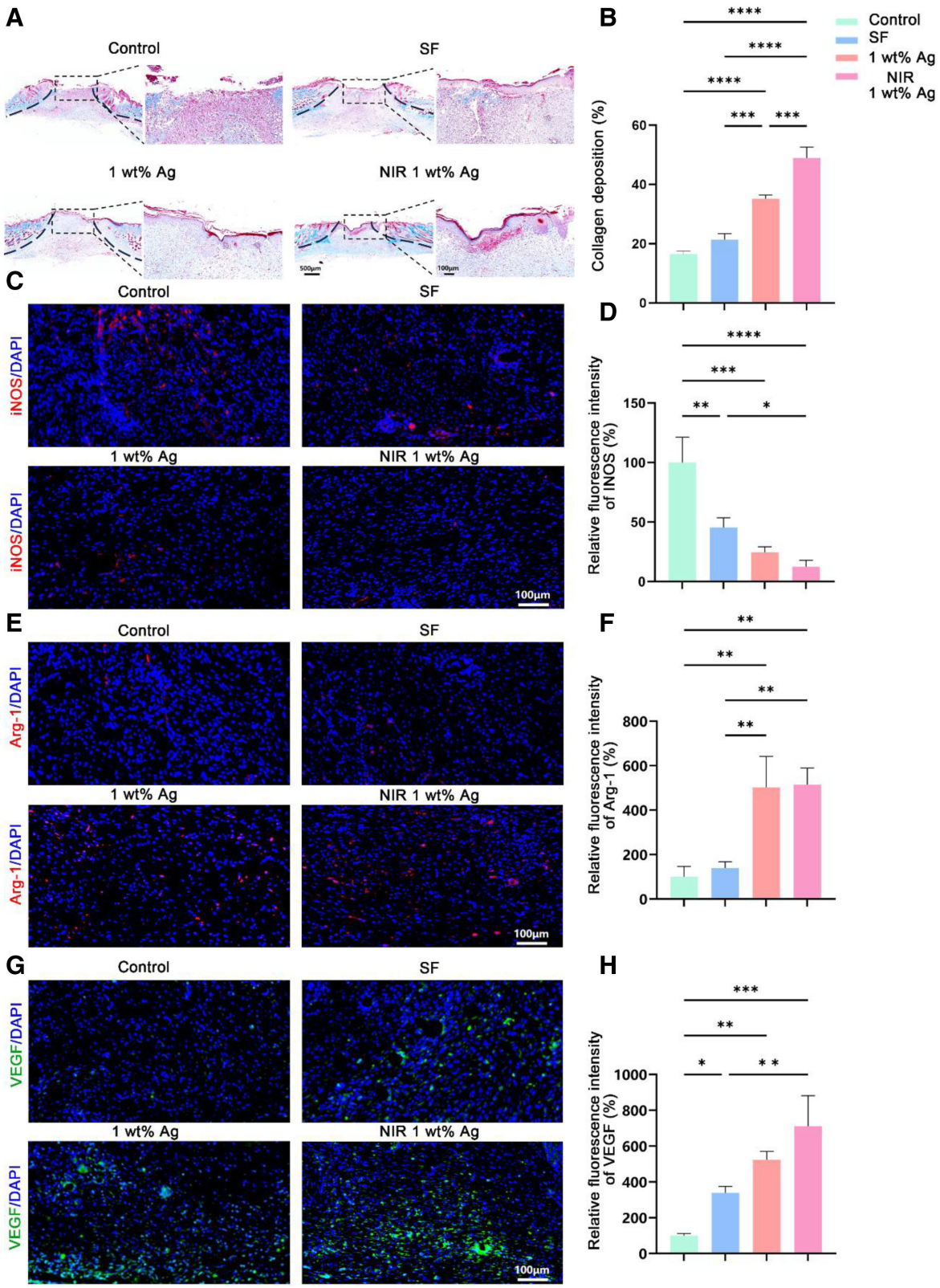

Figure 7. Masson and immunofluorescence staining results. (A, B) Masson staining and quantitative analysis. (C, D) iNOS staining and quantitative analysis. (E, F) Arg-1 staining and quantitative analysis. (G, H) VEGF staining and quantitative analysis.

of cell structure (Figure 5E, F). However, with increasing Ag NWs doping concentrations, the bacteria's surface exhibited shrinkage or rupture, indicating severe damage to the bacterial cell membrane. This further supports the significant role of Ag NWs in PTT.

In conclusion, Ag NWs@SF films not only exhibit excellent antibacterial performance but also enhance their antibacterial activity through photothermal effects. This photothermal synergistic antibacterial mechanism provides a potential therapeutic approach for subsequent in vivo wound healing simulations.

2.8 In vivo infected wound repair

Wound infections pose significant challenges in clinical treatment, particularly when caused by drug-resistant bacteria, as conventional antibiotic therapies often prove inadequate. Wound healing consists of 4 distinct phases: hemostasis, inflammation, proliferation, and remodeling[34]. Infections can disrupt the normal transition between these phases, leading to persistent inflammation and delaying the initiation of proliferation and remodeling, ultimately resulting in slow wound healing and prolonged treatment cycles[35]. Traditional dressings lack objective wound data, rendering clinical assessment heavily dependent on healthcare providers' experience. Additionally, dressing changes increase the risk of secondary injury, posing a significant threat to wound recovery[36]. By leveraging the superior electrical signal response of Ag NWs[37], this system detects subtle physiological changes at and around the wound site, providing quantitative data for evaluating healing progress. Given the complexity of wound healing and infection processes, we developed simulated wound fluid to ensure accurate and reliable monitoring under biologically relevant conditions. The composite membrane demonstrates potential for dynamically tracking wound microenvironmental changes, enabling real-time, data-driven assessment of wound status (Figure 6B).

During normal skin healing, macrophages transition from a proinflammatory (M1) state to an anti-inflammatory (M2) state[38]. This transition is characterized by an increase in the number of M2 macrophages over time, which secrete anti-inflammatory factors that facilitate tissue repair. Conversely, in infected wounds, bacterial infections trigger a robust inflammatory response, resulting in significant infiltration of inflammatory cells, primarily M1 macrophages, which leads to chronic inflammation and impedes tissue repair[39]. Additionally, bacterial infections can damage endothelial cells, inhibiting their proliferation and migration, thereby affecting the formation of new capillaries.

Based on in vitro experimental results, Ag NWs with a doping concentration of 1 wt% were selected for in vivo studies. A full-thickness infected wound model was developed on the backs of mice to investigate the effects of infrared-excited Ag NWs on the healing of infected skin wounds and the underlying mechanisms involved. Figure 6A illustrates the experimental procedures performed at each time point. Under 0.8 W/cm^2 of 808 nm infrared irradiation, the 1 wt% Ag reached the target temperature of 42 °C within 2 min for antibacterial treatment. When continuously irradiated for 10 min, the temperature in the treated region did not exceed 45 °C, thus preventing damage to dermal cells (Figure 6D). The status of wound healing is illustrated in Figure 6E, where the wound area was quantified using ImageJ software, and the wound defects at various time points were overlapped, as shown in Figure 6E. The NIR 1 wt% Ag group exhibited a significant reduction in wound area, with an unhealed area of only 3.9% ± 0.2% at 14 days, markedly superior to the control group, SF group, and 1 wt% Ag group, which had unhealed areas of 14.2% ± 1.9%, 10.5% ± 0.9%, and 8.7% ± 0.7%, respectively ($P < 0.05$) (Figure 6G). Hematoxylin–Eosin (H&E) staining results indicated that the control group had a longer remaining wound length, with epidermal continuity restored to only 72.7%, along with notable infiltration of inflammatory cells and abnormal muscle structures observed in the dermis. The 1 wt% Ag and NIR 1 wt% Ag groups demonstrated effective epidermal healing in the defect area, characterized by the formation of an epidermal stratum corneum, almost no infiltration of inflammatory cells in the dermis, as well as the presence of dermal papillae of the dermis and newly formed hair follicles (Figure 6H–J).

Masson staining and analysis of collagen deposition further revealed that the 1 wt% Ag and NIR 1 wt% Ag groups exhibited enhanced rates of collagen deposition (Figure 7A, B). The persistence of an inflammatory environment is a primary factor contributing to the difficulty of healing infected wounds. This study confirmed the expression of M1 and M2 macrophages through iNOS and Arg-1 staining. Results indicated that at 14 days, compared to the control and SF groups, the 1 wt% Ag and NIR 1 wt% Ag groups significantly reduced the number of proinflammatory M1 macrophages while promoting the transition to anti-inflammatory M2 macrophages (Figure 7C, F). VEGF as a key factor in angiogenesis was also expressed at high levels in the 1 wt% Ag and NIR 1 wt% Ag groups (Figure 7G, H), likely due to the supportive effects of M2 macrophages on endothelial cell migration and proliferation.

Consequently, this study demonstrates that under NIR laser irradiation, Ag NWs generate heat to further enhance antibacterial activity through a synergistic mechanism, promoting the polarization of macrophages from the proinflammatory M1 phenotype to the anti-inflammatory M2 phenotype. This phenotypic transition subsequently influences angiogenesis and tissue repair, thereby facilitating efficient wound healing.

3. Conclusion

In this study, we successfully synthesized Ag NMs with diverse morphologies and sizes, including Ag NWs, Ag NPs, Ag NPs/NGC, and Ag_1/NGC. Among these, Ag NWs were preferentially selected for their superior biological properties, including excellent antioxidant activity, biocompatibility, and potent antibacterial performance. These Ag NWs also promote cell migration, which is essential for wound healing. By incorporating Ag NWs into SF, a biocompatible natural polymer, we developed a composite material that combines the beneficial properties of both components for treating severe infected wounds. The Ag NWs@SF membrane leverages the excellent photoelectric properties of Ag NWs, integrating the responses to NIR light and electrical stimulation, which significantly improves antibacterial efficacy, promotes wound healing, and shows the potential for real-time monitoring of wound changes. This work highlights the distinct advantages of silver nanomaterials with various morphologies and sizes, providing critical insights into the development of advanced wound dressings that address both infection control and tissue regeneration, offering new potential for treating chronic and severe infected wounds.

Acknowledgements

This work was financially supported by National Natural Science Foundation of China (Grant Nos. 52271189 and 32401126), the Science Fund for Distinguished Young Scholars of Shaanxi (Grant No. 2024JC-JCQN-31), the Key Program of enterprises and institutions of Shaanxi Province grant number (Grant No. 2023-LL-QY-44), the Natural Science Foundation of Qinghai Province for Distinguished Young Scholars (Grant No. 2025-ZJ-966J), and the talent youth project of Chinese Academy of Sciences (Grant No. E410GC03).

Conflicts of interests

The authors declare that they have no conflicts of interest.

Author Contributions

Xueqian Li: Writing—original draft, Experimental manipulation, Formal Analysis; Mi Chen: Writing—original draft, Data collation, Conceptualisation; Bingshuai Jing: Investigation; Jie Tian: Software; Huidong Xie: Conceptualisation, Methodology, Software; Hailong Xu: Software; Wenfeng Li: Data collation, Conceptualisation, Software; Mengqi Shen: Conceptualization, Software; Xiaona Ning: Writing—review & editing; Wenhao Zhou: Writing—review & editing; Hu Liu: Writing—review & editing, Funding acquisition, Supervision.

References

[1] Caves E, Horsley V. Reindeer light the way to scarless wound healing. *Cell*. 2022;185:4675–4677.

[2] Uberoi A, McCready-Vangi A, Grice EA. The wound microbiota: microbial mechanisms of impaired wound healing and infection. *Nat Rev Microbiol*. 2024;22:507–521.

[3] Li L, Wang Y, Huang Z, et al. An additive-free multifunctional β-glucan-peptide hydrogel participates in the whole process of bacterial-infected wound healing. *J Control Release*. 2023;362:577–590.

[4] Zhang L, Chen Y, Feng D, et al. Recombinant collagen microneedles for transdermal delivery of antibacterial copper-DNA nanoparticles to treat skin and soft tissue infections. *J Control Release*. 2025;379:191–201.

[5] Li J, Yang Y, Zhang G, et al. Therapeutic advances of magnetic nanomaterials in chronic wound healing. *Nano Today*. 2025;60:102554.

[6] Peng H, Dong D, Feng S, et al. Metal-based antimicrobial agents in wound dressings: infection management and the challenge of antibiotic resistance. *Chem Eng J*. 2025;507:160726.

[7] Gupta A, Ndugire W, Liu L, et al. Bioorthogonal catalysis for antimicrobial therapy. *MedMat*. 2024;1:2–5.

[8] Liu Z, Gao L, Han SY, et al. Bioinspired supramolecular dressing of adaptable programmability and multifunctionality for wound healing. *ACS Appl Mater Interfaces*. 2025;17:13690–13701.

[9] Wang W, Chu F, Zhang W, et al. Silver mineralized protein hydrogel with intrinsic cell proliferation promotion and broad-spectrum antimicrobial properties for accelerated infected wound healing. *Adv Healthcare Mater*. 2024;13:2400047.

[10] Tripathi N, Goshisht MK. Recent advances and mechanistic insights into antibacterial activity, antibiofilm activity, and cytotoxicity of silver nanoparticles. *ACS Appl Bio Mater*. 2022;5:1391–1463.

[11] Hamida RS, Ali MA, Goda DA, et al. Lethal mechanisms of nostoc-synthesized silver nanoparticles against different pathogenic bacteria. *Int J Nanomedicine*. 2020;15:10499–10517.

[12] Terzioğlu E, Arslan M, Balaban BG, et al. Microbial silver resistance mechanisms: recent developments. *World J Microbiol Biotechnol*. 2022;38:158.

[13] Wang CR, Jiang X, Kim H-J, et al. Flexible patch with printable and antibacterial conductive hydrogel electrodes for accelerated wound healing. *Biomaterials*. 2022;285:121479.

[14] Zhang Y, Li Z, Guo H, et al. A biomimetic multifunctional scaffold for infectious vertical bone augmentation. *Adv Sci*. 2024;11:e2310292.

[15] Zhu Y, Wang P, Ma Q, et al. The PVDF-HFP/Ag NWs-based wide electrochemical stability window ecl system for miRNA 21 detection in gastric cancer ascites. *Chem Eng J*. 2023;469:144025.

[16] Li W, Meredov A, Shamim A. Coat-and-print patterning of silver nanowires for flexible and transparent electronics. *Npj Flex Electron*. 2019;3:1–7.

[17] Wu D, Du X, Xue Q, et al. Supramolecular porphyrin photosensitizers based on host–guest recognition for in situ bacteria-responsive near-infrared photothermal therapy. *Adv Healthcare Mater*. 2024;13:2401662.

[18] Sun Q, Tang K, Song L, et al. Covalent organic framework based nanoagent for enhanced mild-temperature photothermal therapy. *Biomater Sci*. 2021;9:7977–7983.

[19] Manivasagan P, Thambi T, Joe A, et al. Progress in nanomaterial-based synergistic photothermal-enhanced chemodynamic therapy in combating bacterial infections. *Prog Mater Sci*. 2024;144:101292.

[20] Yi X, Duan Q-Y, Wu F-G. Low-temperature photothermal therapy: strategies and applications. *Research (Washington, D.C.)*. 2021;2021:9816594.

[21] Gholipourmalekabadi M, Sapru S, Samadikuchaksaraei A, et al. Silk fibroin for skin injury repair: where do things stand? *Adv Drug Deliv Rev*. 2020;153:28–53.

[22] Lv QY, Li QL, Cao P, et al. Designing silk biomaterials toward better future healthcare: the development and application of silk-based implantable electronic devices in clinical diagnosis and therapy. *Adv Mater*. 2025;37:2570068.

[23] Ghosh D, Yaron JR, Abedin MR, et al. Bioactive nanomaterials kickstart early repair processes and potentiate temporally modulated healing of healthy and diabetic wounds. *Biomaterials*. 2024;306:122496.

[24] Haghniaz R, Gangrade A, Montazerian H, et al. An all-in-one transient theranostic platform for intelligent management of hemorrhage. *Adv Sci*. 2023;10:2301406.

[25] Lin D, Li M, Wang L, et al. Multifunctional hydrogel based on silk fibroin promotes tissue repair and regeneration. *Adv Funct Mater*. 2024;34:2405255.

[26] Biswas S, Bhunia BK, Janani G, et al. Silk fibroin based formulations as potential hemostatic agents. *ACS Biomater Sci Eng*. 2022;8:2654–2663.

[27] Ngo PKT, Nguyen DN, Nguyen HP, et al. Silk fibroin/chitosan/montmorillonite sponge dressing: enhancing hemostasis, antimicrobial activity, and angiogenesis for advanced wound healing applications. *Int J Biol Macromol*. 2024;279:135329.

[28] Zhou G, Xu L, Hu G, et al. Nanowires for electrochemical energy storage. *Chem Rev*. 2019;119:11042–11109.

[29] Ali MH, Azad MAK, Khan KA, et al. Analysis of crystallographic structures and properties of silver nanoparticles synthesized using pkl extract and nanoscale characterization techniques. *ACS Omega*. 2023;8:28133–28142.

[30] Liu H, Li X, Zhao X, et al. Large annular dipoles bounded between single-atom Co and Co cluster for clarifying electromagnetic wave absorbing mechanism. *Adv Funct Mater*. 2023;33:2304442.

[31] Torres-López JL, Lázaro-Mass S, Rosa-García SD, et al. Medicinal plants extract for the bio-assisted synthesis of Ag/AgCl nanoparticles with antibacterial activity. *J Clust Sci*. 2024;36:20.

[32] Lee S, Lee J, Byun H, et al. Evaluation of the anti-oxidative and ros scavenging properties of biomaterials coated with epigallocatechin gallate for tissue engineering. *Acta Biomater*. 2021;124:166–178.

[33] Zhou H, He J, Liu R, et al. Microenvironment-responsive metal-phenolic network release platform with ROS scavenging, anti-pyroptosis, and ecm regeneration for intervertebral disc degeneration. *Bioact Mater*. 2024;37:51–71.

[34] Wang Y, Luo M, Li T, et al. Multi-layer-structured bioactive glass nanopowder for multistage-stimulated hemostasis and wound repair. *Bioact Mater*. 2023;25:319–332.

[35] Qi X, Ge X, Chen X, et al. An immunoregulation hydrogel with controlled hyperthermia-augmented oxygenation and ROS scavenging for treating diabetic foot ulcers. *Adv Funct Mater*. 2024;34:2400489.

[36] Ding Y-W, Wang Z-Y, Ren Z-W, et al. Advances in modified hyaluronic acid-based hydrogels for skin wound healing. *Biomater Sci*. 2022;10:3393–3409.

[37] Sekhar SC, Nagaraju G, Yu JS. Conductive silver nanowires-fenced carbon cloth fibers-supported layered double hydroxide nanosheets as a flexible and binder-free electrode for high-performance asymmetric supercapacitors. *Nano Energy*. 2017;36:58–67.

[38] Sharifiaghdam M, Shaabani E, Faridi-Majidi R, et al. Macrophages as a therapeutic target to promote diabetic wound healing. *Mol Ther*. 2022;30:2891–2908.

[39] Dalli J, Chiang N, Serhan C. AB0042 identification of sulfido-conjugated mediators that promote resolution of infection and organ protection. *Ann Rheum Dis*. 2016;75:911.

How to cite this article: Li X, Chen M, Jing B, Tian J, Xie H, Xu H, Li W, Shen M, Ning X, Zhou W, Liu H. Biobased Ag nanowire films with high antibacterial activity for infected wound healing. MedMat 2026;3(1):e00036. doi: 10.1097/mm9.0000000000000036